

***Ground-Based Transmission Spectroscopy with VLT FORS2:
Evidence for faculae and clouds in the optical spectrum of the warm Saturn WASP-110b***

NIKOLAY NIKOLOV ¹, GRACJAN MACIEJEWSKI ², SAVVAS CONSTANTINOU ³, NIKKU MADHUSUDHAN ³,
JONATHAN J. FORTNEY ⁴, BARRY SMALLEY ⁵, AARYNN L. CARTER ⁶, ERNST J. W. DE MOOIJ ⁷,
BENJAMIN DRUMMOND⁸, NEALE P. GIBSON ⁹, CHRISTIANE HELING ^{10,11,12}, NATHAN MAYNE ¹³,
THOMAS MIKAL-EVANS ¹⁴, DAVID K. SING ¹⁵ AND JAMIE WILSON⁷

¹*Space Telescope Science Institute, 3700 San Martin Dr, Baltimore, MD 21218, USA*

²*Institute of Astronomy, Faculty of Physics, Astronomy and Informatics, Nicolaus Copernicus University, ul. Grudziadzka 5, 87-100 Toruń, Poland*

³*Institute of Astronomy, University of Cambridge, Madingley Road, Cambridge, CB3 0HA, UK*

⁴*Department of Astronomy and Astrophysics, University of California, Santa Cruz, CA 95064, USA*

⁵*Astrophysics Group, Keele University, Keele, UK*

⁶*Department of Astronomy and Astrophysics, University of California, Santa Cruz, Santa Cruz, CA 95064, USA*

⁷*Astrophysics Research Centre, School of Mathematics and Physics, Queens University Belfast, Belfast BT7 1NN, UK*

⁸*Met Office, Fitzroy Road, Exeter, EX1 3PB, UK*

⁹*School of Physics, Trinity College Dublin, Dublin 2, Ireland*

¹⁰*Centre for Exoplanet Science, University of St Andrews, North Haugh, St Andrews, KY169SS, UK*

¹¹*SUPA, School of Physics & Astronomy, University of St Andrews, North Haugh, St Andrews, KY169SS, UK*

¹²*SRON Netherlands Institute for Space Research, Sorbonnelaan 2, 3584 CA Utrecht, NL*

¹³*Astrophysics Group, University of Exeter, Exeter, EX4 2QL, UK*

¹⁴*Kavli Institute for Astrophysics and Space Research, Massachusetts Institute of Technology, Cambridge, MA 02139, USA*

¹⁵*Department of Physics and Astronomy, Johns Hopkins University, Baltimore, MD 21218, USA*

(Accepted May 13, 2021)

ABSTRACT

We present a ground-based optical transmission spectrum for the warm Saturn-mass exoplanet WASP-110b from two transit observations made with the FOCAL Reducer and Spectrograph (FORS2) on the Very Large Telescope (VLT). The spectrum covers the wavelength range from 4000 to 8333 Å which is binned in 46 transit depths measured to an averaged precision of 220 parts per million (ppm) over an averaged 80 Å bin for a $V_{\text{mag}} = 12.8$ star. The measured transit depths are unaffected by a dilution from a close A-type field dwarf, which was fully resolved. The overall main characteristic of the transmission spectrum is an increasing radius with wavelength and a lack of the theoretically predicted pressure-broadened sodium and potassium absorption features for a cloud-free atmosphere. We analyze archival high-resolution optical spectroscopy and find evidence for low to moderate activity of the host star, which we take into account in the atmospheric retrieval analysis. Using the AURA retrieval code, we find that the observed transmission spectrum can be best explained by a combination of unocculted stellar faculae and a cloud deck. Transmission spectra of cloud-free and hazy atmospheres are rejected at a high confidence. With a possible cloud deck at its terminator, WASP-110b joins the increasing population of irradiated hot-Jupiter exoplanets with cloudy atmospheres observed in transmission.

Keywords: editorials, notices — miscellaneous — catalogs — surveys

1. INTRODUCTION

Transmission spectroscopy is a powerful tool for constraining the composition and diversity of clear, cloudy and hazy atmospheres of irradiated gas-giant exoplanets. During a planetary transit, part of the starlight filters through the upper planetary atmosphere at the

limb, causing the planetary effective radius to vary with wavelength (transmission spectrum), depending on the atmospheric composition (Seager & Sasselov 2000). Transit observations from both space and the ground have started to reveal a prevalence of clouds and hazes in the atmospheres of these planets across the range of planetary mass, radius and temperature (Pont et al. 2013; Gibson et al. 2013a,b; Sing et al. 2016). Clouds and hazes have strong implications for all aspects of a planet’s atmosphere and affect the observable spectra by effectively reducing the size of absorption features. Why some exoplanets have clear atmospheres while others have atmospheres dominated by hazes or clouds is currently not well understood. Enabling an exploration of the relationship between clouds/hazes and fundamental properties such as mass, radius, temperature, and composition requires a statistically-large sample of exoplanets, which has triggered multiple transmission spectroscopy efforts from space and the ground (Sing et al. 2016, 2019; Wyttenbach et al. 2017; Palle et al. 2017; Rackham et al. 2017; Huitson et al. 2017; Kirk et al. 2018).

In this paper, we present new results for the 4000 – 8333 Å transmission spectrum of WASP110b from a large VLT transmission spectral survey with FORS2, comprising twenty exoplanets. This program rests on an earlier study demonstrating that FORS2 on the VLT is an ideal instrument for exoplanet characterization, capable of distinguishing between a clear, cloudy and hazy hot-Jupiter atmospheres (Nikolov et al. 2016; Gibson et al. 2017; Carter et al. 2020). Initial results from the present large VLT program have so far been presented in Nikolov et al. (2018) for WASP-96b and Wilson et al. (2020) for WASP-103b, revealing a cloud-free atmosphere with sodium abundance constraint and a cloudy atmosphere, respectively.

Detected by the Wide Angle Search for Planets (Pollacco et al. 2006), WASP-110b is a sub-Jupiter transiting exoplanet (planetary mass $M_p = (0.510 \pm 0.064) M_J$, where M_J is the mass of Jupiter, planetary radius $R_p = (1.238 \pm 0.056) R_J$, where R_J is the radius of Jupiter, and equilibrium temperature $T_{eq} = 1,134 \pm 33$ K) orbiting a moderately bright ($V_{mag} = 12.762 \pm 0.092$) G9 star (effective temperature $T_{eff} = 5400 \pm 140$ K, surface gravity $\log g = 4.1 \pm 0.2$ (cgs) and metallicity $[Fe/H] = -0.06 \pm 0.10$) located at a distance of 277 ± 3 pc in the south-eastern part of the constellation Sagittarius (Anderson et al. 2014a; Gaia Collaboration et al. 2018).

This paper is organized as follows. Section 2 and 3 detail our observations. We describe the data reduc-

tion and light curve analysis in Section 4. Results and discussion are presented in Section 5.

2. OBSERVATIONS

2.1. VLT

We observed two primary transits of WASP-110b on UT 2017 June 30th and September 25th with the Focal Reducer and Spectrograph (FORS2, Appenzeller et al. 1998) attached to the Unit Telescope 1 (UT1, Antu) of the Very Large Telescope (VLT) at the European Southern Observatory (ESO) on Cerro Paranal in Chile (Fig. 1) as part of Large Program 199.C-0467 (PI: Nikolov). We used similar observing setup and strategy to our earlier VLT studies (Nikolov et al. 2016; Gibson et al. 2017; Nikolov et al. 2018; Carter et al. 2020; Wilson et al. 2020).

During the two transits, we collected data in multi-object spectroscopy mode with a mask consisting of two broad slits centered on the target and on a reference star of similar brightness. The reference star (known as 2MASS 20234536-4403456) is a bright source in the FORS2 field of view $V_{mag} = 12.999 \pm 0.013$ and is located at an angular separation of $2'.9$ eastward from the target and a distance of 604 ± 14 pc from the Earth. The reference is of higher temperature ($T_{eff} = 5912 \pm 126$ K) with magnitude differences (target minus reference) from the PPMXL and Gaia DR2 catalogues: $\Delta B = -0.36$, $\Delta G = -0.30$, $\Delta V = -0.24$, $\Delta R = -0.35$, $\Delta J = -0.46$, $\Delta H = -0.52$ and $\Delta K = -0.55$ (Roeser et al. 2010; Gaia Collaboration et al. 2018). We used broad slits spanning $22''$ along the dispersion and $\sim 120''$ along the spatial (perpendicular) axis to minimize slit light losses due to seeing variations and guiding imperfections. We observed both transits with the same slit mask and the red detector (Massachusetts Institute of Technology - MIT), which is a mosaic of two chips. We positioned the instrument field of view such that each detector imaged one source. To improve the duty cycle, we made use of the fastest available read-out mode (200 kHz, ~ 30 s). During both nights, we ensured that the Longitudinal Atmospheric Dispersion Corrector (LADC) is in its neutral (park) position, i.e. inactive.

In addition to the bright reference star, a fainter star is located at $\sim 5''$ eastward from WASP-110. The star (known as 6678937482610261632 in the Gaia DR2 catalog) is an A-type dwarf ($T_{eff} = 9617 \pm 128$ K, $M \sim 2.280 M_\odot$, where M_\odot is the mass of the Sun, $R \sim 1.890 R_\odot$, where R_\odot is the radius of the Sun, $\log g \sim 4.2$, luminosity $L \sim 21 L_\odot$, where L_\odot is the luminosity of the Sun) of an apparent brightness of $V_{mag} = 14.992 \pm 0.046$ and $G_{mag} = 14.9710 \pm 0.0006$ at a distance of $4640 \pm$

1237 pc and is not physically associated with the WASP-110 system (Gaia Collaboration et al. 2018). The A-type dwarf is resolved from WASP-110 in the acquisition images and the spectroscopy time series of both nights.

During the first night we monitored the flux of WASP-110 and the comparison star under thin cirrus conditions. We used the dispersive element GRIS600B (hereafter blue), which covers the spectral range from 3600 to 6200 Å at a resolving power $R = \lambda/\Delta\lambda \approx 600$. The field of view rose from an airmass 1.47 to 1.06 and at the end of the observations the field of view was at an airmass of 1.12. The seeing gradually improved from 0.5'' to 0.4'', as measured from a Gaussian fit to the spatial profile of the stellar spectra. We collected a total of 87 exposures for 5h with integration times of 80s and 200s, for the first 11 and remaining 76 exposures.

During the second night, we collected data under photometric conditions. We made use of the dispersive element GRIS600RI (hereafter red), which covers the range from 5400 to 8200 Å, in combination with the GG435 blocking filter to isolate the first order. The field of view rose from an airmass of 1.063 to 1.060 and the observations ended with the target at airmass of 1.853. The seeing varied between 0.3'' and 0.6''. We monitored WASP-110 and the reference star for 4h49m with ~ 8 min interruption at UT 3:33 due to a computer operational issue and collected a total of 154 spectra with integration times between 80 and 100s.

2.2. TESS

WASP-110 was observed by the Transiting Exoplanet Survey Satellite (Ricker et al. 2014, TESS) on Camera 1 CCD 2 during the Extended Mission between 2020 July 04 and 30 (Sector 27) with a 10-minute cadence in the full frame images (FFIs). A light curve was produced using tools available in the Lightkurve v1.9 package (Lightkurve Collaboration et al. 2018) and applied to post-stamps 15×15 pixel ($5.25' \times 5.25'$) wide. They were extracted from FFIs with the TESSCut¹ online tool (Brasseur et al. 2019) with WASP-110 centred in a frame. Fluxes were obtained employing a quadratic aperture which was 3-pixel wide without one corner pixel in order to avoid blending with a nearby bright star. The sky background level was determined with an algorithm based on standard-deviation thresholding. Trends caused by systematic effects or stellar variation were removed with the Savitzky-Golay filter with a window width of 12 hours. Prior to this step, in-transit and

in-occultation data points were masked out using a trial ephemeris.

The final light curve is plotted in the upper panel in Fig 2. Six consecutive transits of WASP-110 b were observed. For further analysis, the individual transit light curves were extracted with time margins equal to ± 2.5 times a transit duration. Their photometric noise rates (Fulton et al. 2011) were found to be between 4.0 and 6.0 parts per thousand (ppth) of the normalised flux per minute of observation. Individual light curves are displayed in the middle and bottom panels in Fig 2.

3. CALIBRATIONS

Our reduction and analysis of the VLT FORS2 data commenced by subtracting a bias frame and by applying a flat field correction to the raw images. We computed a master bias and flat field by obtaining the median of 100 individual frames. We extracted one-dimensional spectra using the Image Reduction and Analysis Facility (IRAF)'s APALL task by performing an unweighted summation. To trace the stars, we used a fit of a Legendre polynomial of two parameters. We removed the sky background by subtracting the median background from the stellar spectrum for each wavelength, computed from a box located away from the spectral trace. We found that aperture radii of 10 pixels and sky regions from 25 to 100 pixels (where the zero point is the middle of the spectrum special profile) minimize the dispersion of the out-of-transit flux of the band-integrated white light curves.

We performed a wavelength calibration of the extracted one-dimensional spectra using spectra of an emission lamp, obtained after each of the two transit observations with a mask identical to the science mask, but with slit widths of 1''. We established a wavelength solution for each of the two stars with a second degree Legendre polynomial fit to the centres of a dozen lines, which we identified by performing a Gaussian fit. To account for displacements during the course of each observation and relative to the reference star, we placed the extracted spectra on a common Doppler-corrected rest frame through cross-correlation. All spectra were found to drift in the dispersion direction to no more than 2.5 pixels, with instrument gravity flexure and differential atmospheric dispersion being the most likely reasons.

Typical spectra of WASP-110 and the reference star are shown in Figure 1. We achieved typical signal-to-noise ratios for the target and reference of 338 and 301 per pixel for the central wavelength of the blue grism and 354 and 306 for the red grism, respectively.

4. LIGHT CURVE ANALYSIS

¹ <https://mast.stsci.edu/tesscut/>

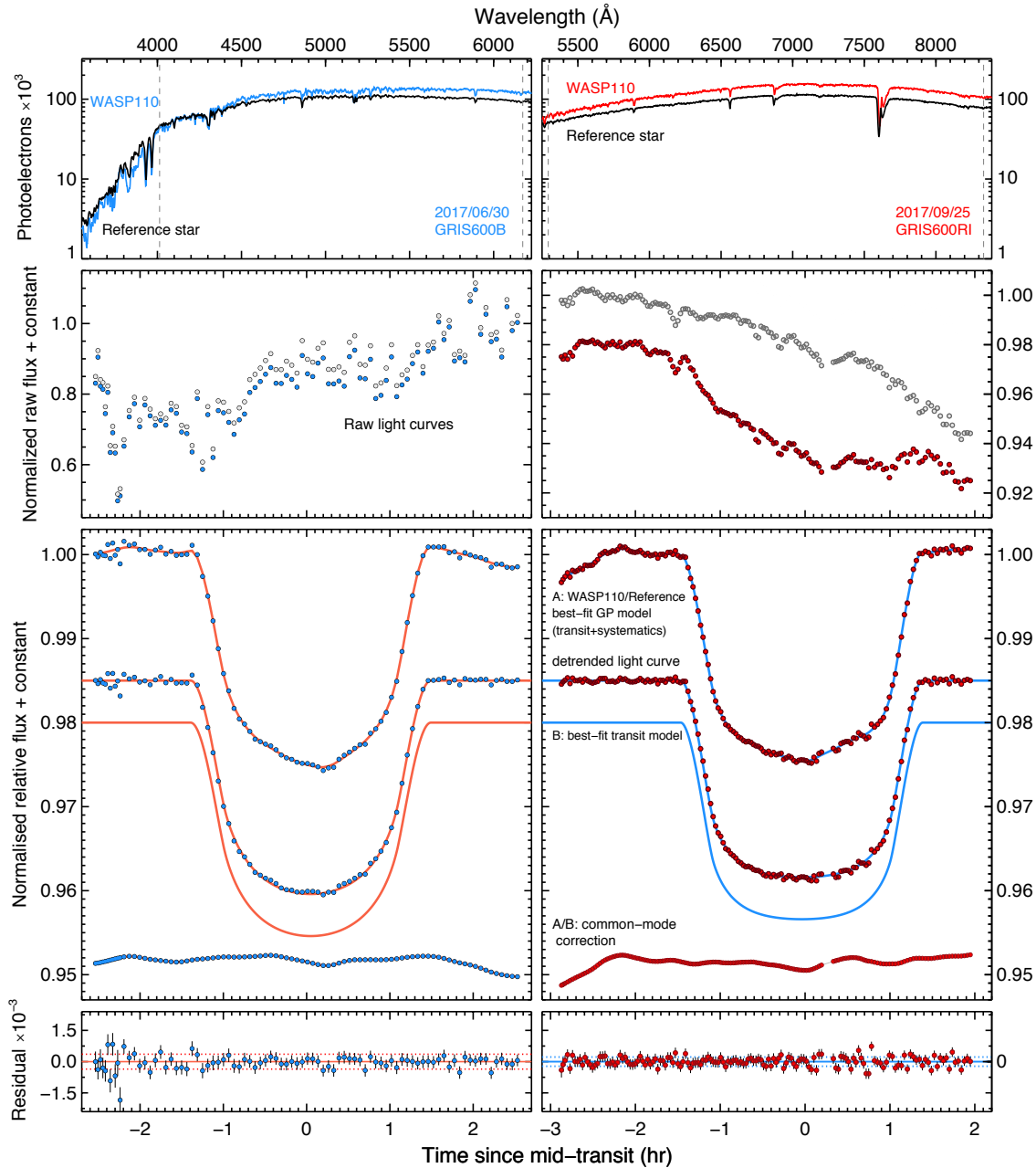


Figure 1. VLT FORS2 stellar spectra and white-light curves compared to models. Left and right panels show the GRIS600B (blue) and GRIS600RI (red) datasets, respectively. The top row shows representative stellar spectra used for calibration with the dashed lines indicating the wavelength region used to produce the white-light curves. The second row shows normalized raw light curves for both target and reference star. The third row shows normalized relative target-to-reference raw flux along with the marginalized Gaussian process model (A), the detrended transit light curve and model (B), and the common-mode correction (A/B). The fourth row shows the best-fit light curve residuals and 1σ error bars, obtained by subtracting the marginalized transit and systematics models from the relative target-to-reference raw flux. The two light curve residuals show dispersions of 380 and 210 parts-per-million, respectively.

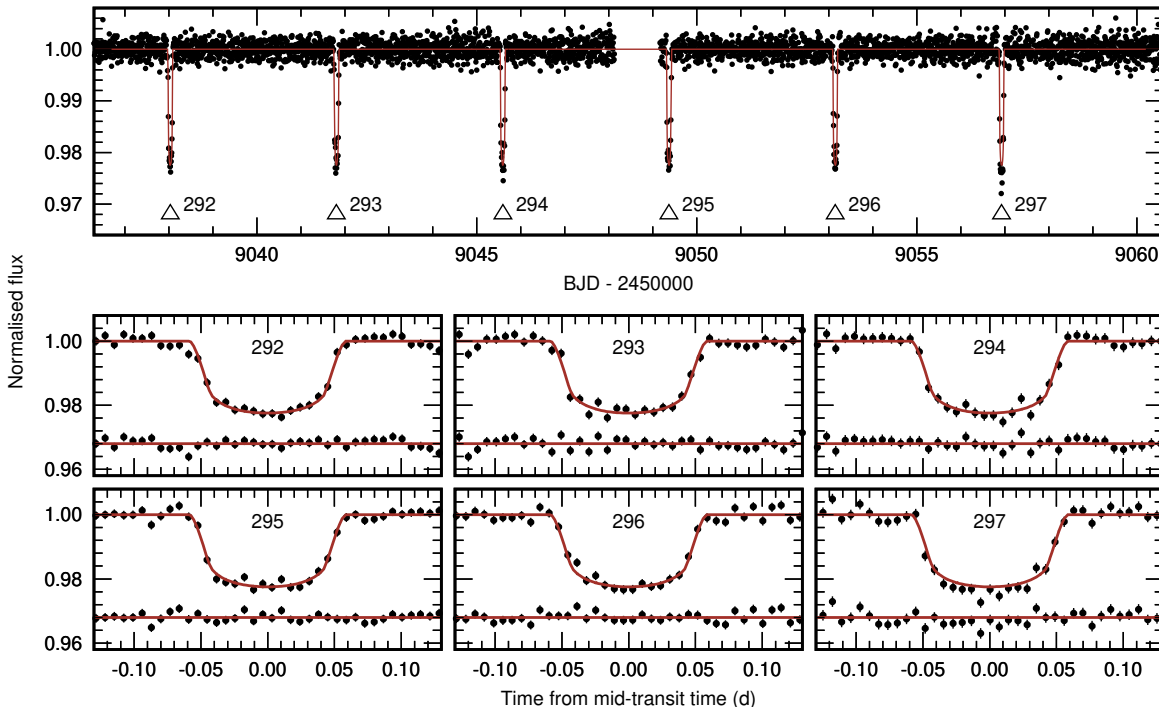


Figure 2. Top panel: De-trended TESS light curve for WASP-110. The mid-transit times are indicated with open triangles and numbered following the ephemeris refined in this paper. The best-fitting transit model is drawn with a red line. Middle and lower panels: the individual transit light curves together with the best-fitting model. The residuals are plotted below each light curve and the vertical bars indicate the 1σ photometric uncertainties.

Our light curve analysis of the VLT data closely follows the approach of [Nikolov et al. \(2018\)](#). For each transit, we produced wavelength-summed ‘white’ and spectroscopic light curves for WASP-110 and the reference star by summing the flux of each spectrum along the dispersion axis. We corrected the light curves for extinction caused by the Earth’s atmosphere by dividing the flux of the target by the flux of the reference star.

4.1. White light curves

We divided the raw flux of the target by the raw flux of the reference star to remove the variations of Earth’s atmospheric transparency, [Figure 1](#). We modeled the transit and systematic effects of the white-light curves by treating the data as a Gaussian process.² and assuming quadratic limb darkening for the star ([Gibson et al. 2012](#)). The transit parameters: mid-time T_{mid} , orbital inclination i , normalized semi-major axis a/R_* (where R_* is the radius of the star), the planet-to-star radius ratio R_p/R_* and the two limb-darkening coefficients u_1 and u_2 were allowed to vary in the fit to each of the two white-light curves, while the orbital period was

held fixed to the previously determined value of [Anderson et al. \(2014a\)](#).

Under the Gaussian process assumption, the data likelihood is a multivariate normal distribution with a mean function μ describing the deterministic transit signal and a covariance matrix K that accounts for stochastic correlations (i.e. poorly constrained systematics) in the light curves:

$$p(\mathbf{f}|\boldsymbol{\theta}, \gamma) = \mathcal{N}(\mu, K), \quad (1)$$

where p is the probability density function, \mathbf{f} and $\boldsymbol{\theta}$ are vectors containing the flux measurements and mean function parameters, respectively; γ is a function containing the covariance parameters and \mathcal{N} is a multivariate normal distribution. The mean function μ is defined as:

$$\mu(\mathbf{t}, \hat{\mathbf{t}}; c_0, c_1, \boldsymbol{\theta}) = [c_0 + c_1 \hat{\mathbf{t}}] T(\mathbf{t}, \boldsymbol{\theta}), \quad (2)$$

where \mathbf{t} is a vector of all central exposure time stamps in Julian Date, $\hat{\mathbf{t}}$ is a vector containing all standardized times, that is, with subtracted mean exposure time and divided by the standard deviation, c_0 and c_1 describe a linear baseline trend, $T(\boldsymbol{\theta})$ is an analytical expression describing the transit and $\boldsymbol{\theta} = (i, a/R_*, T_{\text{mid}}, R_p/R_*, u_1, u_2)$. We made use of the an-

² We made use of the publicly available `george` Gaussian Process Python suite ([Foreman-Mackey 2015](#)).

Table 1. System Parameters

Parameter	Value
Orbital period (day)	3.7783977 (fixed)
Orbital eccentricity	0 (fixed)
<i>GRIS600B</i> , λ (Å)	4013–6173
T_{mid} (MJD)	57934.23238 ^{+0.00026} _{-0.00028}
i (°)	88.00 ^{+0.45} _{-0.37}
a/R_*	10.73 ^{+0.30} _{-0.35}
R_p/R_*	0.1390 ^{+0.0063} _{-0.0064}
u_1	0.52 ^{+0.22} _{-0.24}
u_2	0.61 ^{+0.50} _{-0.47}
$\ln A$	-13.0 ^{+3.3} _{-1.5}
$\ln \eta_{\text{time}}$	-0.9 ^{+2.7} _{-1.5}
c_0	1.0000 ^{+0.0011} _{-0.0018}
c_1	-0.00032 ^{+0.0010} _{-0.0007}
<i>GRIS600RI</i> , λ (Å)	5293–8333
T_{mid} (MJD)	58021.13912 ^{+0.00025} _{-0.00023}
i (°)	88.52 ^{+0.67} _{-0.46}
a/R_*	11.19 ^{+0.21} _{-0.20}
R_p/R_*	0.1389 ^{+0.0041} _{-0.0044}
u_1	0.18 ^{+0.25} _{-0.22}
u_2	0.74 ^{+0.40} _{-0.44}
$\ln A$	-12.4 ^{+3.3} _{-1.3}
$\ln \eta_{\text{time}}$	-0.7 ^{+2.4} _{-1.2}
c_0	1.0014 ^{+0.0013} _{-0.0027}
c_1	0.00097 ^{+0.0017} _{-0.00080}
<i>Weighted mean:</i>	
i (°)	88.16 ^{+0.37} _{-0.32}
a/R_*	11.07 ^{+0.18} _{-0.17}
<i>GRIS600B</i>	(fixed i , a/R_* , T_{mid})
R_p/R_*	0.1435 ^{+0.0047} _{-0.0036}
u_1	0.66 ^{+0.14} _{-0.16}
u_2	0.19 ^{+0.20} _{-0.19}
<i>GRIS600RI</i>	(fixed i , a/R_* , T_{mid})
R_p/R_*	0.1396 ^{+0.0033} _{-0.0037}
u_1	0.12 ^{+0.20} _{-0.17}
u_2	0.68 ^{+0.20} _{-0.24}

alytical formulae of Mandel & Agol (2002); Kreidberg (2015).

We computed the theoretical values of the coefficients of the quadratic limb darkening law using a three-dimensional stellar atmosphere model grid (Magic et al. 2015), factored by the throughputs of the blue and red grisms. In these calculations, we adopted the closest match to the effective temperature, surface gravity and metallicity of the exoplanet host star found in Ander-

son et al. (2014a). The choice of a quadratic versus a more complex law (such as a four-parameter nonlinear law) was motivated by the study of Espinoza & Jordán (2016), in which the two-parameter law has been shown to introduce negligible bias on the measured properties of transiting systems similar to WASP-110. The quadratic law also requires a much shorter computational time to compute model transit light curve. The theoretical limb darkening coefficients were employed as priors in our light curve fits.

Similar to our earlier VLT studies, we defined the covariance matrix as $K = \sigma_i^2 \delta_{ij} + k_{ij}$, where σ_i contains the photon noise uncertainties, δ_{ij} is the Kronecker delta function and k_{ij} is a covariance function. The white noise term σ_w was assumed to have the same value for all data points and was allowed to freely vary. We chose to use the Matérn $\nu = 3/2$ kernel with time t for the covariance function. Our kernel choice is motivated by the study of Gibson et al. (2013b), where the Matérn $\nu = 3/2$ kernel is empirically motivated using simulated data, and is the first to use this kernel for light curve analysis. We also experimented by adding additional terms, including the spectral dispersion and cross-dispersion drifts x and y as input variables, and the full-width at half-maximum (FWHM) measured from the cross-dispersion profiles of the two-dimensional spectra and the speed of the rotation angle z . As with the linear time term, we also standardized the input parameters before the light curve fitting. We chose to use the time for both observations instead of combinations of other terms, because a GP of time resulted in well-behaved residuals. The covariance function was defined as:

$$k_{ij} = A^2 (1 + \sqrt{3}D_{ij}) \exp(-\sqrt{3}D_{ij}), \quad (3)$$

where A is the characteristic correlation amplitude and

$$D_{ij} = \sqrt{\frac{(\hat{t}_i - \hat{t}_j)^2}{\tau_t^2}}, \quad (4)$$

where τ_t is the correlation length scale and the hatted variables are standardized. The parameters $\mathbf{X} = (c_0, c_1, T_{\text{mid}}, i, a/R_*, R_p/R_*, u_1, u_2)$ and $\mathbf{Y} = (A, \tau_t)$ were allowed to vary and fixed the orbital period P to its literature value. Uniform priors were adopted for \mathbf{X} and log-uniform priors for \mathbf{Y} .

We marginalized the posterior distribution $p(\theta, \gamma|f) \propto p(f|\theta, \gamma)p(\theta, \gamma)$ using the Markov chain Monte Carlo software package emcee Foreman-Mackey et al. (2013). We identified the maximum likelihood solution using the Levenberg–Marquardt least-squares algorithm (Marquardt 2009) and initialized three groups of 150 walk-

ers close to that maximum. The first two groups were run for 350 samples and the third one for 4,500 samples. To ensure faster convergence, we re-sampled the positions of the walkers in a narrow space around the position of the best walker from the first run before running for the second group. This helps prevent some of the walkers starting in a low-likelihood area of parameter space, which can require more computational time to converge. Figure 1 and Table 1 show transit models for each of the two observations computed using the marginalized posterior distributions and the fitted parameters, respectively. We find residual dispersion of 378 and 223 parts per million for the blue and red light curves, respectively.

We computed the weighted mean values of i and a/R_* and repeated the fits allowing only R_p/R_* , u_1 and u_2 to vary. We held fixed i and a/R_* to the weighted mean values and the two central times, T_{mid} were held fixed to the values determined from the first fit. We report our results in Table 1.

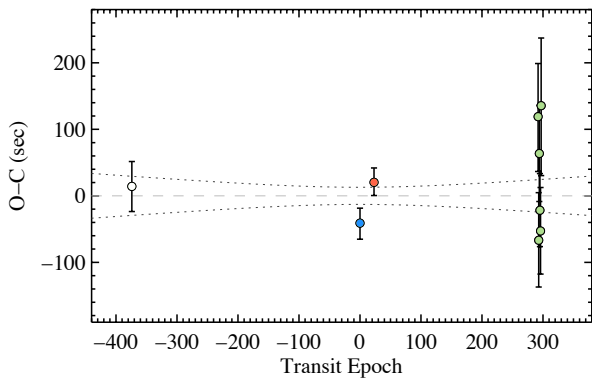


Figure 3. Observed minus computed (O-C) transit times based on the best-fitting orbital period and central transit time derived from our analysis of the Euler (white dot), VLT (blue and red dots) and TESS (green dots) light curves. The error bars and dotted lines indicate the 1σ uncertainties of the transit times and derived ephemeris, respectively.

4.2. TESS light curves and transit ephemeris

The TESS light curves were used to refine the transit ephemeris for WASP-110b. In addition, we used a follow-up photometric time series from the discovery paper (Anderson et al. 2014b). This early epoch observation was acquired on 2013 August 16 with the 1.2-m Euler-Swiss telescope equipped in the EulerCam photometer. In total, 121 measurements were collected in a Cousins I filter with a median cadence of 137 s. The photometric noise rate was found to be 1.15 ppth per minute of observation. The original timestamps in HJD_{UTC}

Table 2. Central transit times

Epoch	Central time, BJD _{TDB}	O-C, day
-374	242456521.61682 ± 0.00044	0.000164
0	242457934.73824 ± 0.00028	-0.000475
23	242458021.64217 ± 0.00023	0.000235
292	242459038.03324 ± 0.00095	0.001378
293	242459041.80949 ± 0.00081	-0.000773
294	242459045.58940 ± 0.00084	0.000736
295	242459049.36682 ± 0.00063	-0.000251
296	242459053.14486 ± 0.00075	-0.000611
297	242459056.9254 ± 0.0012	0.001569

were converted into BJD_{TDB} using an online applet³ (Eastman et al. 2010). For timing purposes, we do not correct the TESS transit light curves for the third-light contamination. Thus, we used fluxes prior the dilution correction applied in (Anderson et al. 2014b).

The mid-transit times were determined by fitting a trial transit model with the Transit Analysis Package (TAP, Gazak et al. (2012)). The TESS and EulerCam light curves were modelled simultaneously with the orbital inclination, the semi-major axis scaled in star radii, and the ratio of planet to star radii linked together. The limb darkening (LD) effect was approximated with a quadratic law, the coefficients of which were bi-linearly extrapolated from tables of Claret & Bloemen (2011). The coefficients for the TESS passband were calculated as averages of R , I , and Sloan Digital Sky Survey z' values. Their values were allowed to vary under the Gaussian penalties with a conservative width of 0.1. Possible trends in the time domain were accounted for using second order polynomials for each transit light curve. The best-fitting values and their uncertainties were calculated as the medians and 15.9 and 84.1 percentiles of the marginalised posteriori probability distributions generated from 10 MCMC chains, each 10^6 steps long with 10% burn-in phase. The results are given in Table 2.

We converted to BJDs the central transit times from our VLT observations and combined these with the BJD TDB central times from our Euler and TESS light curve analysis and computed an updated transit ephemeris. We fitted a linear function of the orbital period (P) and transit epoch (E): $T_C(E) = T_0 + EP$. We find a period of $P = 3.77840121 \pm 0.00000082$ (d) and a mid-transit time of $T_C = 2457934.73871 \pm 0.00015$ (d). The updated ephemeris is in agreement with the ephemeris reported

³ <http://astrutils.astronomy.ohio-state.edu/time/hjd2bjd.html>

by Anderson et al. (2014a) and does not indicate the presence of transit timing variations (TTVs) Figure 3.

4.3. Spectroscopic light curve analyses

To produce spectroscopic light curves, we summed the flux of the target and reference star in bands with variable widths from 80 to 253 Å, Table 4. The blue and red grisms overlap in the wavelength range from 5,300 to 6,200 Å and each covers the sodium D lines at 5,890 and 5,896 Å. We choose common bins within the overlapping region to allow a direct comparison when combining the blue and red transmission spectra. We enlarged the first three bins in the blue grism and merged two pairs of bins, covering the O₂ A and B telluric bands from 7,594 to 7,621 Å and from 6,867 to 6,884 Å, respectively. In this way, we increased the signal-to-noise ratio of the broader bands and produced a total of 46 light curves.

We established wavelength-independent, i.e. common mode systematic correction factors for each night, similar to our previous studies with FORS2 (Nikolov et al. 2016; Gibson et al. 2017; Nikolov et al. 2018; Carter et al. 2020; Wilson et al. 2020). To obtain the correction factors, we divided the white-light curve from each night by the transit model computed with the weighted-mean system parameters (Section 4.1). The common mode factors for each night are shown in Figure 1.

We modeled the spectroscopic light curves with a function accounting for the transit and systematics simultaneously. Before fitting, we divided each spectroscopic light curve by the wavelength-independent systematic correction factors for that night. In the fits, we allowed only the relative planet radius, R_p/R_* and the linear limb-darkening coefficient u_1 to vary. We obtained theoretical values for u_1 and u_2 following the same approach as for the white light curves. We also fitted for both limb-darkening coefficients and found that the uncertainty of u_2 is large and consistent with the theoretical prediction. We interpret this as an indication for insufficient constraining power of the data for the quadratic coefficient. Given the transmission spectra did not substantially change we chose to fix u_2 and to fit only for u_1 .

We accounted for the systematics using a low-order polynomial (up to a second degree with no cross terms) of dispersion and cross-dispersion drift, air mass, FWHM and the rate of change of the rotator angle. We produced all possible combinations of detrending variables and performed separate fits including each combination within the systematics function. This approach has been preferred as opposed to GP regression, as the CM-corrected VLT spectroscopic light curves exhibit a lower level of systematic effects. Our choice also rests

on results from a VLT comparative follow-up of WASP-39b with atmospheric features detected with the *Hubble Space Telescope* (Nikolov et al. 2016). We computed the Akaike Information Criterion for each fit and estimated the statistical weight of the model depending on the number of degrees of freedom, (Akaike 1974). We chose to rely on the Akaike Information Criterion instead of other information criteria, for example, the Bayesian Information Criterion (Schwarz 1978), because the Akaike Information Criterion selects more complex models, resulting in more conservative error estimates. We marginalized the resulting relative radii and linear limb-darkening coefficient following Gibson 2014. We found that for most light curves systematics models parameterized with linear air mass, dispersion drift and FWHM terms resulted in the highest statistical weight.

Before fitting each light curve, we set the spectrophotometric uncertainties of each band to values that include photon and readout noise. To determine the best-fit models, we used a Levenberg–Marquardt least-squares algorithm and rescaled the uncertainties of the fitted parameters using the dispersion of the residuals, (Markwardt 2009). Residual outliers larger than 3σ , typically 2-3 per light curve, were excluded from the analysis. Correlated residual red noise was accounted following the methodology of Pont et al. (2006) by modeling the binned variance with the relation $\sigma^2 = \sigma_w^2/N + \sigma_r^2$ relation, where σ_w is the uncorrelated white noise component, N is the number of measurements in the bin and σ_r is the red noise component. We found white noise dispersion in the range from about 450 to 900 parts per million. For the red noise, we found a dispersion in the range from about 40 to 70 parts per million.

4.4. Stellar Activity and Variability Monitoring

Activity and rotation are known to complicate the interpretation of transmission spectra and in particular when combining multi-instrument, multi-epoch data sets (Huitson et al. 2013; McCullough et al. 2014; Pinhas et al. 2018). To assess the level of stellar activity and photometric variability, we inspected the cores of the Ca II H&K lines and photometry time series from archival data. We analyzed five MPG/ESO 2.2-metre telescope high-resolution spectra obtained with the FEROS spectrograph (ESO program: 099.A-9010, PI P. Sarkis) at a resolution of $R = \lambda/\delta\lambda = 48,000$, Table 3. The spectra have been obtained using a fiber with a diameter of 2 arcsec and reduced with ESO’s FEROS pipeline to phase 3 products, i.e. extracted one-dimensional spectra with wavelength solution. A comparison between the tabulated and observed wave-

lengths of the Ca II H&K line cores indicates an offset (Figure 5). This can be attributed to the low signal-to-noise of the individual spectra, which reach ~ 5 in the blue wavelengths, but can also be an indication for the presence of emission in the core of the lines. The activity index, S_{HK} , was estimated from the spectrum using the method described by Vaughan et al. (1978) and transformed to the $\log R'_{\text{HK}}$ system using the relations from Noyes et al. (1984). We measure $\log R'_{\text{HK}} = -4.9^{+0.09}_{-0.24}$, which is consistent with low to moderate activity of the host star.

We analyzed an archival light curve consisting of 250 photometric data points from the Ohio State University’s All-sky Automated Survey for Supernovae (ASAS-SN) Photometry Database, Shappee et al. (2014); Jayasinghe et al. (2019). The data has been obtained during the period from May to December 2014 and from March to December in the years from 2015 to 2018, respectively (Figure 12). We performed Lomb-Scargle periodogram analysis with trial frequencies ranging between 0.005 and 1 d^{-1} , corresponding to a period range between 1 and 200 d. We find a rotational modulation with a period of 13.74 d with a false alarm probability (FAP) of ~ 0.25 . We phase-folded the photometry and fitted a sinusoid to measure the amplitude of the flux variation. We found an amplitude of $0.5 \pm 0.1\%$ and residual scatter of 12.8 parts-per-thousand (ppt), Figure 4. Our result agrees with the 4 mmag (0.4%) upper limit for flux variability of WASP-110 reported by Anderson et al. (2014a). Anderson et al. (2014a) also found that WASP-110 is an evolved 8.6 ± 3.5 Gyr G9 star, which implies a gyrochronologic rotation comparable or exceeding the equatorial rotation period of the Sun i.e., $\gtrsim 25$ days. Anderson et al. (2014a) report $v \sin(i_*) = 0.2 \pm 0.6 \text{ km s}^{-1}$, which translates to a rotation period $P_*(i_* = 90^\circ) \gtrsim 34$ days. While this is a discrepancy with our finding, a detailed comparison is hampered by the unconstrained stellar axial tilt, which can significantly decrease the actual rotation period. It is worth mentioning that empirical relations of the rotation periods to the chromospheric activity level $\log R'_{\text{HK}}$ predict ~ 22 days for WASP-110 (Suárez Mascareño et al. 2015, their Figure 13). Given the spread of ~ 10 days in the empirical relationship for the rotation period for G-type stars with $-0.1 < [\text{Fe}/\text{H}] < 0.1$, the predicted estimate is consistent with our measured period. This is also the case for $v \sin(i_* \sim 4^\circ)$ of Anderson et al. (2014a).

4.5. Results

The measured transmission spectrum of WASP-110b is presented in Figure 6 and 7. To combine the transmis-

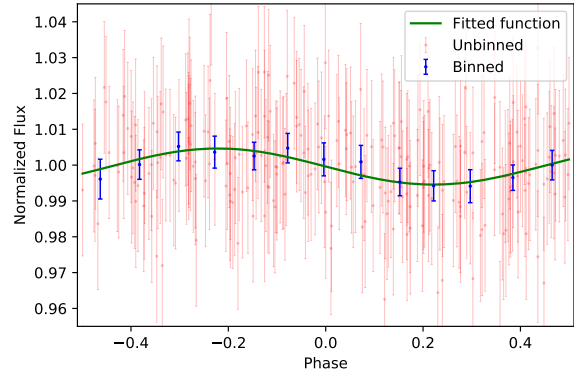


Figure 4. ASAS-SN photometry phase-folded with the highest significance period found from our periodogram analysis. Plotted are the unbinned photometry (red), binned (blue) and the best-fit sine function (green). The vertical bars represent 1σ uncertainties.

Table 3. FEROS observing log

Date	Exposure	Airmass	Seeing	S/N in
2017 (UT)	time (s)		(arcsec)	0.03Å bin
May 14	3,000	1.209	1.72	24.2
May 17	2,400	1.178	< 0.91	24.8
June 02	1,200	1.042	1.15	27.7
July 21	1,200	1.035	0.92	25.4
July 21	1,200	1.035	0.91	25.2

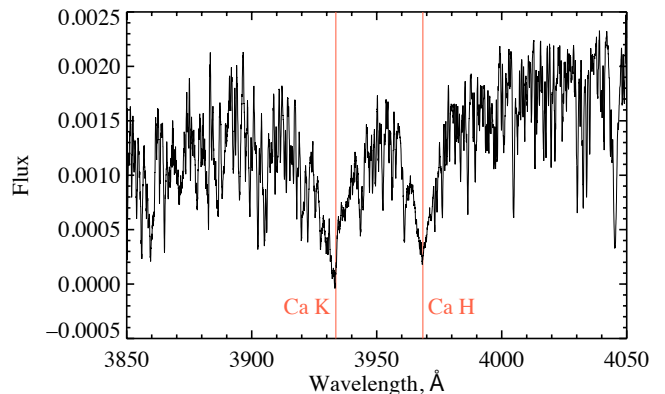


Figure 5. Combined FEROS spectra around the Ca II H&K lines for WASP-110. The laboratory central wavelength of each line are indicated with the red continuous lines.

sion spectra from the blue and red grism observations, we computed the weighted mean of both datasets within the overlapping wavelength region. We find a marginally significant $\sim 1.5\sigma$ radius difference from the two obser-

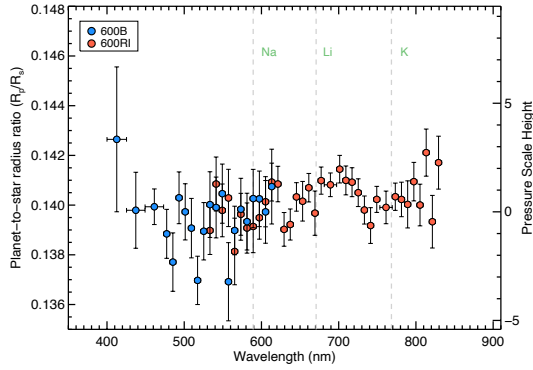


Figure 6. Indicated are the VLT FORS2 relative planet-to-star radius measurements from grism 600B (blue dots) and 600RI (red dots) along with the 1σ uncertainties.

variations of $\Delta R_p/R_* = (33 \pm 22) \times 10^{-4}$. This corresponds to a depth variation of ~ 11 ppm, which is within the $0.5 \pm 0.1\%$ stellar variation of the ASAS-SN photometry. The blue and red pairs of radius measurements show an excellent agreement within the overlapping region.

The spectrum is marginally flat without an increased absorption from sodium or potassium, which are the main absorbers expected in the optical transmission spectra of irradiated gas giants at $T_{eq} \sim 1100$ K similar to WASP-110b. An increased absorption is present in the wavelength range from ~ 0.63 to $\sim 0.75 \mu\text{m}$, spanning ~ 3 pressure scale heights. To interpret the spectrum we turn to model comparison and retrieval analysis.

5. DISCUSSION

5.1. Comparison to forward models

We compared the transmission spectrum with clear, cloudy and hazy synthetic spectra with solar abundances from the model presented in Fortney et al. (2008, 2010). These spectra include a self-consistent treatment of radiative transfer and chemical equilibrium of neutral and ionic species. Chemical mixing ratios and opacities were computed assuming solar metallicity and local chemical equilibrium, accounting for condensation and thermal ionization but not photoionization (Lodders 1999, 2002; Freedman et al. 2008, 2014).

Similar to our previous studies, the cloudy and hazy models were computed using a simplified treatment of the scattering and absorption to simulate the effect of small particle haze aerosols and large particle cloud condensates at optical and near-infrared wavelengths. In the case of haze, Rayleigh scattering opacity ($\sigma = \sigma_0(\lambda/\lambda_0)^{-4}$) has been assumed with a cross-section which was $1,000\times$ the cross-section of molecular hydrogen gas ($\sigma_0 = 5.31 \times 10^{-27} \text{ cm}^2$ at $\lambda_0 = 3,500 \text{ \AA}$ (Lodders 1999)). To account for the effects of a flat cloud deck, we

Table 4. Transmission spectrum of WASP-110b

Wavelength, \AA	R_p/R_*	u_1	u_2
4000 – 4253	0.14265 ± 0.00291	0.882 ± 0.030	0.042
4253 – 4493	0.13979 ± 0.00153	0.819 ± 0.018	0.104
4493 – 4733	0.13993 ± 0.00072	0.745 ± 0.011	0.150
4733 – 4813	0.13884 ± 0.00099	0.721 ± 0.018	0.182
4813 – 4893	0.13771 ± 0.00118	0.679 ± 0.022	0.251
4893 – 4973	0.14029 ± 0.00104	0.660 ± 0.021	0.216
4973 – 5053	0.13973 ± 0.00113	0.673 ± 0.019	0.197
5053 – 5133	0.13907 ± 0.00120	0.696 ± 0.021	0.163
5133 – 5213	0.13697 ± 0.00097	0.672 ± 0.021	0.188
5213 – 5293	0.13895 ± 0.00115	0.597 ± 0.022	0.256
5293 – 5373	0.13934 ± 0.00078	0.599 ± 0.023	0.248
5373 – 5453	0.14043 ± 0.00081	0.574 ± 0.021	0.262
5453 – 5533	0.14009 ± 0.00079	0.610 ± 0.021	0.236
5533 – 5613	0.13911 ± 0.00093	0.610 ± 0.022	0.246
5613 – 5693	0.13869 ± 0.00079	0.570 ± 0.021	0.260
5693 – 5773	0.13969 ± 0.00070	0.536 ± 0.026	0.285
5773 – 5853	0.13919 ± 0.00076	0.542 ± 0.022	0.267
5853 – 5933	0.13964 ± 0.00078	0.520 ± 0.026	0.288
5933 – 6013	0.13978 ± 0.00068	0.485 ± 0.023	0.294
6013 – 6093	0.13998 ± 0.00079	0.502 ± 0.027	0.290
6093 – 6173	0.14089 ± 0.00068	0.493 ± 0.027	0.283
6173 – 6253	0.14085 ± 0.00071	0.415 ± 0.020	0.303
6253 – 6333	0.13902 ± 0.00068	0.428 ± 0.019	0.296
6333 – 6413	0.13922 ± 0.00062	0.405 ± 0.019	0.307
6413 – 6493	0.14033 ± 0.00057	0.360 ± 0.019	0.308
6493 – 6573	0.14015 ± 0.00080	0.363 ± 0.019	0.334
6573 – 6653	0.14070 ± 0.00057	0.369 ± 0.018	0.321
6653 – 6733	0.13968 ± 0.00089	0.394 ± 0.023	0.309
6733 – 6813	0.14099 ± 0.00055	0.353 ± 0.020	0.303
6813 – 6973	0.14082 ± 0.00048	0.346 ± 0.016	0.309
6973 – 7053	0.14145 ± 0.00055	0.290 ± 0.020	0.315
7053 – 7133	0.14099 ± 0.00058	0.310 ± 0.024	0.309
7133 – 7213	0.14092 ± 0.00058	0.302 ± 0.024	0.303
7213 – 7293	0.14050 ± 0.00056	0.312 ± 0.021	0.315
7293 – 7373	0.13980 ± 0.00056	0.309 ± 0.024	0.316
7373 – 7453	0.13918 ± 0.00072	0.336 ± 0.026	0.310
7453 – 7533	0.14023 ± 0.00052	0.303 ± 0.021	0.316
7533 – 7693	0.13991 ± 0.00066	0.297 ± 0.020	0.319
7693 – 7773	0.14034 ± 0.00055	0.276 ± 0.024	0.313
7773 – 7853	0.14023 ± 0.00069	0.289 ± 0.025	0.321
7853 – 7933	0.14003 ± 0.00095	0.257 ± 0.027	0.317
7933 – 8013	0.14094 ± 0.00078	0.271 ± 0.026	0.314
8013 – 8093	0.14000 ± 0.00084	0.291 ± 0.022	0.312
8093 – 8173	0.14211 ± 0.00095	0.272 ± 0.026	0.317
8173 – 8253	0.13933 ± 0.00106	0.247 ± 0.025	0.313
8253 – 8333	0.14171 ± 0.00107	0.278 ± 0.025	0.313

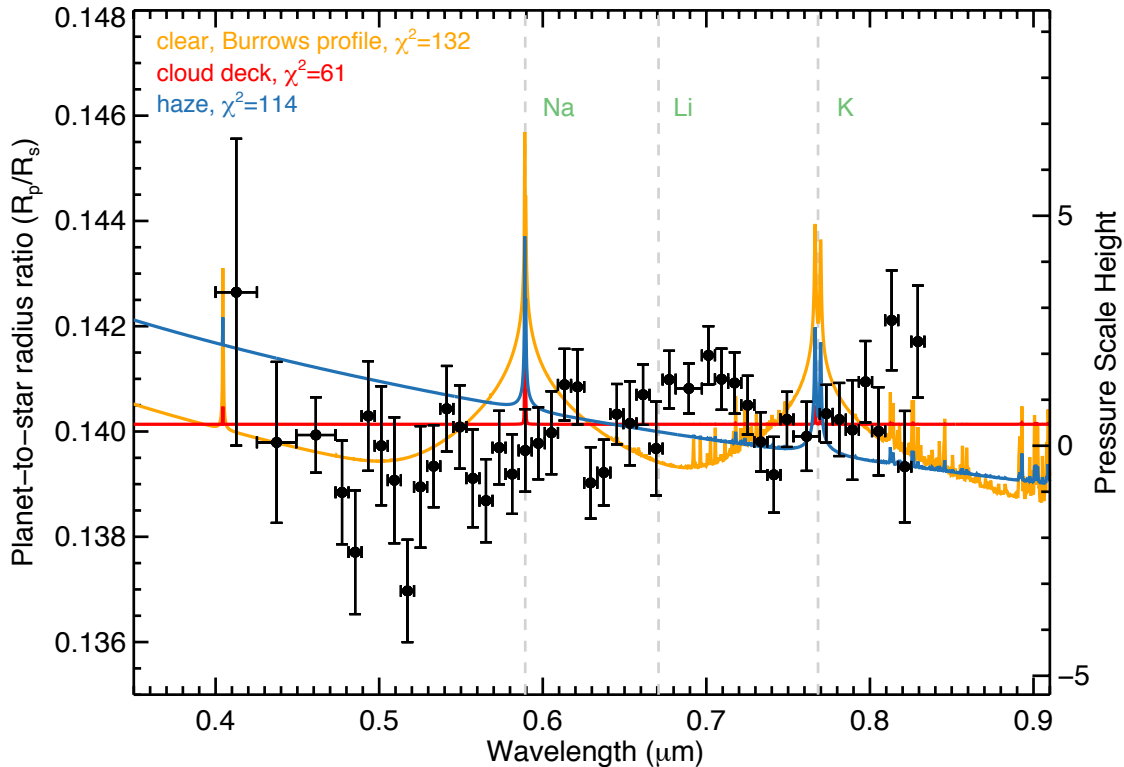


Figure 7. Shown is the VLT transmission spectrum (black dots with 1σ vertical error bars; the horizontal bars indicate spectral bin widths) compared with a clear, cloudy and hazy one-dimensional forward atmospheric spectra at solar abundance (continuous lines). Line broadening shapes for Na and K have been calculated from the prescription detailed in (Burrows et al. 2000). Synthetic spectra with hazes or clouds (blue and red) predict much smaller and narrower absorption features.

included a wavelength-independent cross-section, which was a factor of $100\times$ the cross-section of molecular hydrogen gas at $\lambda_0 = 3,500\text{\AA}$.

We obtained the average values of the models within the wavelength bins of the observed transmission spectrum and fitted these theoretical values to the data with a single parameter accounting for their vertical offset. The χ^2 and Bayesian Information Criterion (BIC) statistic quantities were computed for each synthetic spectrum with the number of degrees of freedom for each model determined by $\nu = N - m$, where N is the number of measurements and m is the number of free parameters in the fit. We find the cloudy spectra to best describe our observations ($\chi^2 = 61$) followed by the haze and cloud-free simulated spectra (Figure 7)

5.2. Retrieval analysis

We additionally considered inverse methods to constrain the atmospheric properties of WASP-110b via atmospheric retrievals using the AURA code (Pinhas et al. 2018). AURA computes model transmission spectra using line-by-line radiative transfer in a plane parallel atmosphere in hydrostatic equilibrium. The forward model-generating component is interfaced with

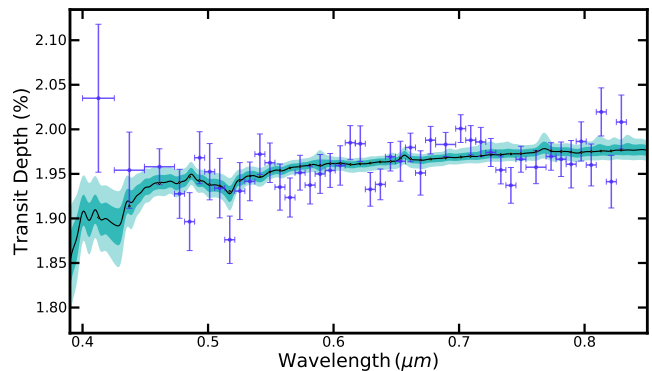


Figure 8. Our VLT FORS2 data (blue errorbars) and the retrieved median spectrum (black) and corresponding 1- and 2- σ contours (dark and light turquoise) from our AURA retrieval. The median spectral fit has an increasing transit depth with wavelength, due to faculae on the unobstructed stellar surface. It does not have any significant absorption features from chemical species.

the PyMultiNest Nested Sampling package (Buchner et al. 2014), which allows for Bayesian parameter estimation and model comparison. We describe the terminator pressure-temperature profile using the 6-parameter prescription of Madhusudhan & Seager (2009). Our

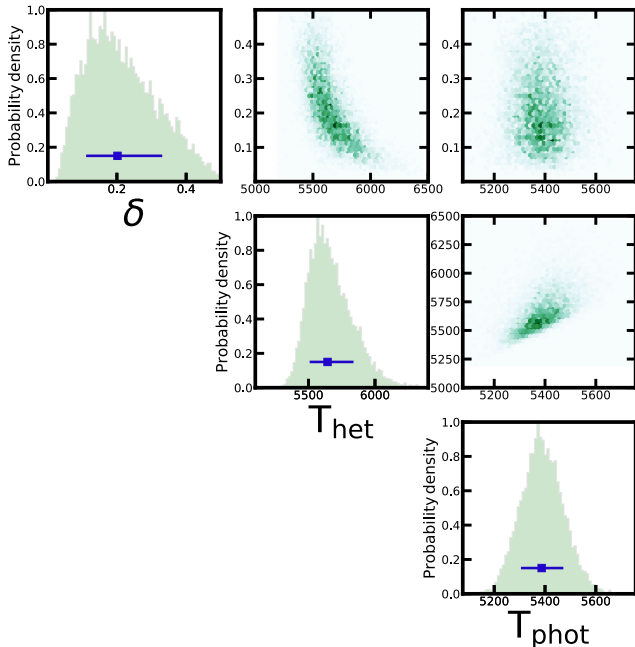


Figure 9. The posterior probability distributions for the three stellar heterogeneity parameters used in our AURA retrieval. Our retrieval successfully constrains all three. We retrieved a T_{het} estimate that is higher than both the literature T_{eff} and retrieved T_{phot} values, indicating that hotter faculae are the dominant form of stellar heterogeneity.

model atmosphere includes opacities arising from H_2 - H_2 and H_2 -He collision-induced absorption, as well as absorption from H_2O (Rothman et al. 2010), Na and K (Welbanks et al. 2019), the latter two accounting for the effects of pressure broadening. We avoid including high temperature species in our atmospheric model (e.g. TiO, VO and other metal hydrides/oxides, ions, etc), given the relatively low equilibrium temperature of WASP-110 b. Inhomogeneous coverage of clouds and hazes is incorporated in our model using the prescription of Pinhas et al. (2018), treating clouds as grey opacity below the cloud deck and hazes as a modification to Rayleigh scattering above the cloud deck.

AURA also incorporates the effects of stellar heterogeneity, being the first retrieval code demonstrated to successfully include such effects (Pinhas et al. 2018). The stellar heterogeneities are described using 3 parameters: δ , the fraction of the projected stellar disc covered by cooler starspots/hotter faculae, T_{het} the temperature of the starspots/faculae and T_{phot} the temperature of the immaculate photosphere. We construct the spectral contributions of the two stellar surface components by interpolating through a grid of PHOENIX spectra (Husser et al. 2013), fixing the stellar metallicity and gravity to literature values. Hotter faculae/cooler

starspots result in a larger/smaller apparent stellar radius towards the blue end of the spectrum, which in turn results in lower/higher observed transit depths at shorter wavelengths.

We find that our retrieval produces a good fit to the data, as show in Figure 8. We successfully obtain constraints for the three stellar heterogeneity parameters, finding $\delta = 0.20^{+0.13}_{-0.09}$, $T_{\text{het}} = 5643^{+195}_{-134}$ K and $T_{\text{phot}} = 5387^{+85}_{-81}$ K. We show the retrieved posterior distribution for these three parameters in Figure 9. Our retrieved T_{het} value is higher than both the retrieved T_{phot} and literature T_{eff} values, indicating the presence of hotter faculae. We determined the detection significance (D.S.) for stellar heterogeneity by carrying out a Bayesian model comparison with the findings of a second retrieval that excludes the effects of stellar heterogeneity. We find a D.S. of 3.1σ , indicating a strong detection. This stems from the overall trend in the data of increasing transit depths at longer wavelengths, which are attributed to unocculted stellar faculae rather than opacity sources in the planetary atmosphere.

We additionally consider separate retrievals for the grism 600B and 600RI datasets, without applying any offsets to either. We find that the constraints on the cloud and heterogeneity parameters are governed primarily by the 600RI dataset, with the 600B dataset providing only weak constraints. The constraints from both datasets are consistent with each other and with the joint dataset to within the $1\text{-}\sigma$ uncertainties. We, therefore, find that the two datasets can be combined for a joint retrieval with a single set of heterogeneity parameters without significant loss of information.

Our retrieval is unable to detect any of the chemical species considered, including H_2O . We additionally obtain weak constraints for a high-altitude cloud deck pressure, $\log(P_{\text{cloud}}) = -3.4^{+1.8}_{-1.3}$ (in bar), while also finding that our retrieval shows a preference for near-full cloud coverage fractions. As before, we conducted a third retrieval, this time excluding clouds and hazes to determine their D.S.. We find that our retrievals detect clouds and hazes with a 2.1σ significance, suggesting only a tentative detection. Clouds are only tentatively detected because a featureless spectrum can be caused by either clouds or low abundances of alkali metals. The overall posterior distribution is shown in Figure 13.

We also conduct further retrievals to explore how more elaborate model considerations affect our findings. In one case, we additionally consider several chemical species with significant optical opacities, such as TiO, VO and AlO (Fortney et al. 2008; Gandhi & Madhusudan 2019), even though they are not expected in thermochemical equilibrium at the low atmospheric temper-

atures of WASP-110 b. While we find nominal indications of these species, none has a D.S. greater than 2σ to constituting a strong detection. We also run retrievals with an offset applied to either the 600RI or 600B datasets as an additional retrieved parameter. In this case, the D.S. of the heterogeneity is reduced to $\sim 1-2\sigma$, depending on which of the two datasets is being offset, while clouds and hazes are detected at a D.S. of $\sim 2\sigma$.

6. A COMPARISON TO A SIMILAR IRRADIATED EXOPLANET

Atmospheric temperature and gravity are two fundamental properties considered to play a definitive role in the formation of clouds and hazes. With a growing sample of irradiated gas giants characterized in transmission, it becomes imperative to identify similar exoplanets and compare their spectra and physical characteristics. Similar properties have the potential to reveal transitions of atmospheric types and ultimately identify the factors determining why some planets appear cloud-free and others cloudy or hazy. The physical properties of WASP-110b and WASP-6b are nearly identical, which also holds for their host stars (Table 5). With a surface gravity of $\sim 8 \text{ ms}^{-2}$ and an atmospheric temperature estimated to $\lesssim 1200 \text{ K}$, the transmission spectra for both atmospheres are predicted to be dominated by the pressure-broadened absorption features of sodium and potassium. This partially holds for WASP-6b, where observations of *HST* and VLT reveal absorption from sodium, potassium and water and an optical to infrared slope spanning ~ 8 scale heights (Carter et al. 2020). However, with a lack of the theoretically predicted pressure broadened sodium and potassium absorption features, the spectrum of WASP-110b drastically differs from the spectrum of WASP-6b and this difference may likely be attributed to the impact of clouds.

Despite the remarkable similarities in their physical properties, the significant difference in the optical spectra for both planets indicate that additional factors are responsible for determining the presence of clouds and hazes. One such factor is the temperature-pressure profile at the day-night terminator, which can be specific for the west and east limbs. A step toward capturing these effects consistently would involve three-dimensional (3D) simulations that include clouds (e.g. Lines et al. 2018), chemical kinetics (e.g. Drummond et al. 2020), etc., and should start with virtually the same inputs. Given that planetary atmospheres are complex and nonlinear systems, subtle variations from planet to planet, including measured system properties (mass, radius, metallicity), higher-order properties

Table 5. Physical properties

Property	WASP-110b ^A	WASP-6b ^B
Atm. type	<i>cloudy</i>	<i>hazy</i>
Constituent	-	Na, K, H ₂ O
H, km	536	533
T_{eq} , K	1134 ± 33	1184 ± 16
g , m s^{-2}	7.60 ± 1	7.96 ± 0.30
M_p , M_J	0.510 ± 0.064	0.485 ± 0.027
R_p , M_J	1.238 ± 0.056	1.230 ± 0.035
P, day	3.78	3.36
a, au	0.05	0.04
e	$0_{-0}^{+0.61}$	$0.054_{-0.014}^{+0.018}$
T_{eff} , K	5360 ± 130	5375 ± 65
$\log g$, cgs	4.498 ± 0.022	4.487 ± 0.017
[Fe/H]	-0.06 ± 0.10	-0.15 ± 0.09
M_* , M_{\odot}	0.892 ± 0.072	0.836 ± 0.063
R_* , M_{\odot}	0.881 ± 0.035	0.864 ± 0.024
$\log R'_{\text{HK}}$	$-4.9_{-0.24}^{+0.09}$	-4.511 ± 0.037

NOTE—A: Anderson et al. (2014a); B: Gillon et al. (2009).

(gravitational and magnetic fields) and at levels below the precisions achieved by transmission spectroscopy observations reported in Table 4 can result in significantly different atmosphere signals. Furthermore, planetary atmospheres could be time variable, as seen in general circulation models (GCMs) and our own solar system, e.g. oscillations in Earth’s history into Snowball states, global storms on Mars triggered by subtle effects etc. Future observations, including with *JWST* instruments (e.g. MIRI) are expected constrain the planet temperature and shed more light on the composition of the clouds and hazes of exoplanet atmospheres (Wakeford & Sing 2015).

While WASP-110 and WASP-6 are two alike stars with respect to their fundamental physical properties, WASP-6 exhibits a higher level of chromospheric activity, as revealed by the higher $\log R'_{\text{HK}}$ index. Active stars undergoing magnetic cycles modulate cosmic ray fluxes, which can exceed the rate of galactic cosmic rays in the vicinity of the star. The formation of clouds enhances in the presence of a nucleation particle, including liquid or solid particles, such as droplets or grains as they act as nuclei for further condensation (de Pater & Lissauer 2015). Galactic and solar cosmic rays, mainly protons, reaching Earth’s atmosphere carry enough energy to ionize volatile compounds causing them to condense into droplets, or aerosols and enhance cloud formation

(Svensmark 1998; Kirkby 2007; Svensmark et al. 2009; Kirkby et al. 2011). Due to the higher activity level of the host star, it would be natural to assume that WASP-6b experiences a higher flux of cosmic rays and more nucleation events that promote cloud formation in its atmosphere. Planetary magnetic fields are considered to play a shielding role from high energy particles and reduce the formation of nucleation particles and clouds. Could WASP-6b possess a magnetic field that shields its atmosphere and reduces the flux of cosmic rays while WASP-110b’s magnetic field is much weaker? Understanding the global picture of exoplanet atmospheres requires the full asset of planetary physical properties including the planetary magnetic field, which are expected to be probed with the next generation of instruments and would help elucidate the picture toward these two exoplanet atmospheres.

7. SUMMARY

We have conducted a comparative forward and retrieval analysis of the 0.4 to 0.833 μm transmission spectrum of WASP-110b, obtained using VLT FORS2 transit spectroscopy (Section 2.1). We have improved the planet orbital ephemerides and found no departures from the predicted transit times from analysis of six transits observed by the TESS space-based photometer (Section 2.2). We determined the host star exhibits low to moderate activity ($\log R'_{\text{HK}} = -4.9^{+0.09}_{-0.24}$) using optical high-resolution MPG/ESO2.2 FEROS spectroscopy (Section 4.4).

We have compared the VLT transmission spectrum to a set of clear, cloudy and hazy forward hot Jupiter atmosphere spectra (Section 5.1). This analysis indicates a cloudy atmosphere. We have performed retrieval analysis with the AURA retrieval framework, which includes contamination from stellar heterogeneity (Section 5.2). The fiducial model from the retrieval analyses is an excellent fit to the transmission spectrum. The retrieval results point toward a scenario of unocculted faculae

with temperature $\sim 200\text{K}$ hotter than the stellar photosphere and fractional coverage of $\sim 20\%$ in combination with a cloud deck as the explanation for the observed VLT spectrum.

ACKNOWLEDGMENTS

Based on observations made with ESO Telescopes at the La Silla Paranal Observatory under programme ID 199.C-0467 and 099.A-9010. The authors are grateful to Dr. David Anderson and Dr. David Brown for sharing the follow-up light curve with us. GM acknowledges the financial support from the National Science Centre, Poland through grant no. 2016/23/B/ST9/00579. The authors are grateful to Néstor Espinoza, Jayesh Goyal, Ryan MacDonald and Joanna Barstow for the valuable discussions, which helped to improve the manuscript. The authors are grateful to the anonymous reviewer for their constructive comments on the manuscript. This work has made use of data from the European Space Agency (ESA) mission *Gaia* (<https://www.cosmos.esa.int/gaia>), processed by the *Gaia* Data Processing and Analysis Consortium (DPAC, <https://www.cosmos.esa.int/web/gaia/dpac/consortium>). Funding for the DPAC has been provided by national institutions, in particular the institutions participating in the *Gaia* Multilateral Agreement. This work made use of the Python Gaussian process library George. NM acknowledges funding from the UKRI Future Leaders Scheme (MR/T040866/1), Science and Technology Facilities Council Consolidated Grant (ST/R000395/1) and Leverhulme Trust research project grant (RPG-2020-82).

Software: george (Foreman-Mackey 2015), TESSCut tool (Brazzini et al. 2019), Lightkurve v1.9 (Lightkurve Collaboration et al. 2018), TAP, Gazak et al. (2012), IRAF (Tody 1986, 1993), hjd2bjd.html (Eastman et al. 2010), MPFIT (Markwardt 2009), Astropy (Astropy Collaboration et al. 2013, 2018), AURA (Pinhas et al. 2018), PyMultiNest (Buchner et al. 2014)

Facilities: VLT(FORS2), TESS, MPG/ESO2.2(FEROS)

REFERENCES

- Akaike, H. 1974, IEEE Transactions on Automatic Control, 19, 716
- Anderson, D. R., Brown, D. J. A., Collier Cameron, A., et al. 2014a, arXiv e-prints, arXiv:1410.3449. <https://arxiv.org/abs/1410.3449>
- . 2014b, arXiv e-prints, arXiv:1410.3449. <https://arxiv.org/abs/1410.3449>
- Appenzeller, I., Fricke, K., Fürstig, W., et al. 1998, The Messenger, 94, 1
- Astropy Collaboration, Robitaille, T. P., Tollerud, E. J., et al. 2013, A&A, 558, A33, doi: 10.1051/0004-6361/201322068
- Astropy Collaboration, Price-Whelan, A. M., Sipőcz, B. M., et al. 2018, AJ, 156, 123, doi: 10.3847/1538-3881/aabc4f

- Brasseur, C. E., Phillip, C., Fleming, S. W., Mullally, S. E., & White, R. L. 2019, *Astrocut: Tools for creating cutouts of TESS images*. <http://ascl.net/1905.007>
- Buchner, J., Georgakakis, A., Nandra, K., et al. 2014, *A&A*, 564, A125, doi: [10.1051/0004-6361/201322971](https://doi.org/10.1051/0004-6361/201322971)
- Burrows, A., Marley, M. S., & Sharp, C. M. 2000, *ApJ*, 531, 438, doi: [10.1086/308462](https://doi.org/10.1086/308462)
- Carter, A. L., Nikolov, N., Sing, D. K., et al. 2020, *MNRAS*, 494, 5449, doi: [10.1093/mnras/staa1078](https://doi.org/10.1093/mnras/staa1078)
- Claret, A., & Bloemen, S. 2011, *A&A*, 529, A75, doi: [10.1051/0004-6361/201116451](https://doi.org/10.1051/0004-6361/201116451)
- de Pater, I., & Lissauer, J. J. 2015, *Planetary Sciences*
- Drummond, B., Hébrard, E., Mayne, N. J., et al. 2020, *A&A*, 636, A68, doi: [10.1051/0004-6361/201937153](https://doi.org/10.1051/0004-6361/201937153)
- Eastman, J., Siverd, R., & Gaudi, B. S. 2010, *PASP*, 122, 935, doi: [10.1086/655938](https://doi.org/10.1086/655938)
- Espinoza, N., & Jordán, A. 2016, *MNRAS*, 457, 3573, doi: [10.1093/mnras/stw224](https://doi.org/10.1093/mnras/stw224)
- Foreman-Mackey, D. 2015, *George: Gaussian Process regression*, *Astrophysics Source Code Library*. <http://ascl.net/1511.015>
- Foreman-Mackey, D., Hogg, D. W., Lang, D., & Goodman, J. 2013, *PASP*, 125, 306, doi: [10.1086/670067](https://doi.org/10.1086/670067)
- Fortney, J. J., Lodders, K., Marley, M. S., & Freedman, R. S. 2008, *ApJ*, 678, 1419, doi: [10.1086/528370](https://doi.org/10.1086/528370)
- Fortney, J. J., Shabram, M., Showman, A. P., et al. 2010, *ApJ*, 709, 1396, doi: [10.1088/0004-637X/709/2/1396](https://doi.org/10.1088/0004-637X/709/2/1396)
- Freedman, R. S., Lustig-Yaeger, J., Fortney, J. J., et al. 2014, *ApJS*, 214, 25, doi: [10.1088/0067-0049/214/2/25](https://doi.org/10.1088/0067-0049/214/2/25)
- Freedman, R. S., Marley, M. S., & Lodders, K. 2008, *ApJS*, 174, 504, doi: [10.1086/521793](https://doi.org/10.1086/521793)
- Fulton, B. J., Shporer, A., Winn, J. N., et al. 2011, *AJ*, 142, 84, doi: [10.1088/0004-6256/142/3/84](https://doi.org/10.1088/0004-6256/142/3/84)
- Gaia Collaboration, Brown, A. G. A., Vallenari, A., et al. 2018, *A&A*, 616, A1, doi: [10.1051/0004-6361/201833051](https://doi.org/10.1051/0004-6361/201833051)
- Gandhi, S., & Madhusudhan, N. 2019, *MNRAS*, 485, 5817, doi: [10.1093/mnras/stz751](https://doi.org/10.1093/mnras/stz751)
- Gazak, J. Z., Johnson, J. A., Tonry, J., et al. 2012, *Advances in Astronomy*, 2012, 697967, doi: [10.1155/2012/697967](https://doi.org/10.1155/2012/697967)
- Gibson, N. P. 2014, *MNRAS*, 445, 3401, doi: [10.1093/mnras/stu1975](https://doi.org/10.1093/mnras/stu1975)
- Gibson, N. P., Aigrain, S., Barstow, J. K., et al. 2013a, *MNRAS*, 428, 3680, doi: [10.1093/mnras/sts307](https://doi.org/10.1093/mnras/sts307)
- . 2013b, *MNRAS*, 436, 2974, doi: [10.1093/mnras/stt1783](https://doi.org/10.1093/mnras/stt1783)
- Gibson, N. P., Aigrain, S., Roberts, S., et al. 2012, *MNRAS*, 419, 2683, doi: [10.1111/j.1365-2966.2011.19915.x](https://doi.org/10.1111/j.1365-2966.2011.19915.x)
- Gibson, N. P., Nikolov, N., Sing, D. K., et al. 2017, *MNRAS*, 467, 4591, doi: [10.1093/mnras/stx353](https://doi.org/10.1093/mnras/stx353)
- Gillon, M., Anderson, D. R., Triaud, A. H. M. J., et al. 2009, *A&A*, 501, 785, doi: [10.1051/0004-6361/200911749](https://doi.org/10.1051/0004-6361/200911749)
- Huitson, C. M., Désert, J. M., Bean, J. L., et al. 2017, *AJ*, 154, 95, doi: [10.3847/1538-3881/aa7f72](https://doi.org/10.3847/1538-3881/aa7f72)
- Huitson, C. M., Sing, D. K., Pont, F., et al. 2013, *MNRAS*, 434, 3252, doi: [10.1093/mnras/stt1243](https://doi.org/10.1093/mnras/stt1243)
- Husser, T. O., Wende-von Berg, S., Dreizler, S., et al. 2013, *A&A*, 553, A6, doi: [10.1051/0004-6361/201219058](https://doi.org/10.1051/0004-6361/201219058)
- Jayasinghe, T., Stanek, K. Z., Kochanek, C. S., et al. 2019, *MNRAS*, 485, 961, doi: [10.1093/mnras/stz444](https://doi.org/10.1093/mnras/stz444)
- Kirk, J., Wheatley, P. J., Louden, T., et al. 2018, *MNRAS*, 474, 876, doi: [10.1093/mnras/stx2826](https://doi.org/10.1093/mnras/stx2826)
- Kirkby, J. 2007, *Surveys in Geophysics*, 28, 333, doi: [10.1007/s10712-008-9030-6](https://doi.org/10.1007/s10712-008-9030-6)
- Kirkby, J., Curtius, J., Almeida, J., et al. 2011, *Nature*, 476, 429, doi: [10.1038/nature10343](https://doi.org/10.1038/nature10343)
- Kreidberg, L. 2015, *PASP*, 127, 1161, doi: [10.1086/683602](https://doi.org/10.1086/683602)
- Lightkurve Collaboration, Cardoso, J. V. d. M. a., Hedges, C., et al. 2018, *Lightkurve: Kepler and TESS time series analysis in Python*. <http://ascl.net/1812.013>
- Lines, S., Mayne, N. J., Boutle, I. A., et al. 2018, *A&A*, 615, A97, doi: [10.1051/0004-6361/201732278](https://doi.org/10.1051/0004-6361/201732278)
- Lodders, K. 1999, *ApJ*, 519, 793, doi: [10.1086/307387](https://doi.org/10.1086/307387)
- . 2002, *ApJ*, 577, 974, doi: [10.1086/342241](https://doi.org/10.1086/342241)
- Madhusudhan, N., & Seager, S. 2009, *ApJ*, 707, 24, doi: [10.1088/0004-637X/707/1/24](https://doi.org/10.1088/0004-637X/707/1/24)
- Magic, Z., Chiavassa, A., Collet, R., & Asplund, M. 2015, *A&A*, 573, A90, doi: [10.1051/0004-6361/201423804](https://doi.org/10.1051/0004-6361/201423804)
- Mandel, K., & Agol, E. 2002, *ApJL*, 580, L171, doi: [10.1086/345520](https://doi.org/10.1086/345520)
- Markwardt, C. B. 2009, in *Astronomical Society of the Pacific Conference Series*, Vol. 411, *Astronomical Data Analysis Software and Systems XVIII*, ed. D. A. Bohlender, D. Durand, & P. Dowler, 251. <https://arxiv.org/abs/0902.2850>
- McCullough, P. R., Crouzet, N., Deming, D., & Madhusudhan, N. 2014, *ApJ*, 791, 55, doi: [10.1088/0004-637X/791/1/55](https://doi.org/10.1088/0004-637X/791/1/55)
- Nikolov, N., Sing, D. K., Gibson, N. P., et al. 2016, *ApJ*, 832, 191, doi: [10.3847/0004-637X/832/2/191](https://doi.org/10.3847/0004-637X/832/2/191)
- Nikolov, N., Sing, D. K., Fortney, J. J., et al. 2018, *Nature*, 557, 526, doi: [10.1038/s41586-018-0101-7](https://doi.org/10.1038/s41586-018-0101-7)
- Noyes, R. W., Hartmann, L. W., Baliunas, S. L., Duncan, D. K., & Vaughan, A. H. 1984, *ApJ*, 279, 763, doi: [10.1086/161945](https://doi.org/10.1086/161945)
- Palle, E., Chen, G., Prieto-Arranz, J., et al. 2017, *A&A*, 602, L15, doi: [10.1051/0004-6361/201731018](https://doi.org/10.1051/0004-6361/201731018)
- Pinhas, A., Rackham, B. V., Madhusudhan, N., & Apai, D. 2018, *MNRAS*, 480, 5314, doi: [10.1093/mnras/sty2209](https://doi.org/10.1093/mnras/sty2209)

- Pollacco, D. L., Skillen, I., Collier Cameron, A., et al. 2006, *PASP*, 118, 1407, doi: [10.1086/508556](https://doi.org/10.1086/508556)
- Pont, F., Sing, D. K., Gibson, N. P., et al. 2013, *MNRAS*, 432, 2917, doi: [10.1093/mnras/stt651](https://doi.org/10.1093/mnras/stt651)
- Pont, F., Zucker, S., & Queloz, D. 2006, *MNRAS*, 373, 231, doi: [10.1111/j.1365-2966.2006.11012.x](https://doi.org/10.1111/j.1365-2966.2006.11012.x)
- Rackham, B., Espinoza, N., Apai, D., et al. 2017, *ApJ*, 834, 151, doi: [10.3847/1538-4357/aa4f6c](https://doi.org/10.3847/1538-4357/aa4f6c)
- Ricker, G. R., Winn, J. N., Vanderspek, R., et al. 2014, in *Society of Photo-Optical Instrumentation Engineers (SPIE) Conference Series*, Vol. 9143, *Space Telescopes and Instrumentation 2014: Optical, Infrared, and Millimeter Wave*, ed. J. Oschmann, Jacobus M., M. Clampin, G. G. Fazio, & H. A. MacEwen, 914320, doi: [10.1117/12.2063489](https://doi.org/10.1117/12.2063489)
- Roeser, S., Demleitner, M., & Schilbach, E. 2010, *AJ*, 139, 2440, doi: [10.1088/0004-6256/139/6/2440](https://doi.org/10.1088/0004-6256/139/6/2440)
- Rothman, L., Gordon, I., Barber, R., et al. 2010, *JQSRT*, 111, 2139, doi: <https://doi.org/10.1016/j.jqsrt.2010.05.001>
- Schwarz, G. 1978, *Annals of Statistics*, 6, 461
- Seager, S., & Sasselov, D. D. 2000, *ApJ*, 537, 916, doi: [10.1086/309088](https://doi.org/10.1086/309088)
- Shappee, B. J., Prieto, J. L., Grupe, D., et al. 2014, *ApJ*, 788, 48, doi: [10.1088/0004-637X/788/1/48](https://doi.org/10.1088/0004-637X/788/1/48)
- Sing, D. K., Fortney, J. J., Nikolov, N., et al. 2016, *Nature*, 529, 59, doi: [10.1038/nature16068](https://doi.org/10.1038/nature16068)
- Sing, D. K., Lavvas, P., Ballester, G. E., et al. 2019, *AJ*, 158, 91, doi: [10.3847/1538-3881/ab2986](https://doi.org/10.3847/1538-3881/ab2986)
- Suárez Mascareño, A., Rebolo, R., González Hernández, J. I., & Esposito, M. 2015, *MNRAS*, 452, 2745, doi: [10.1093/mnras/stv1441](https://doi.org/10.1093/mnras/stv1441)
- Svensmark, H. 1998, *PhRvL*, 81, 5027, doi: [10.1103/PhysRevLett.81.5027](https://doi.org/10.1103/PhysRevLett.81.5027)
- Svensmark, H., Bondo, T., & Svensmark, J. 2009, *Geophys. Res. Lett.*, 36, L15101, doi: [10.1029/2009GL038429](https://doi.org/10.1029/2009GL038429)
- Tody, D. 1986, in *Society of Photo-Optical Instrumentation Engineers (SPIE) Conference Series*, Vol. 627, *Instrumentation in astronomy VI*, ed. D. L. Crawford, 733, doi: [10.1117/12.968154](https://doi.org/10.1117/12.968154)
- Tody, D. 1993, in *Astronomical Society of the Pacific Conference Series*, Vol. 52, *Astronomical Data Analysis Software and Systems II*, ed. R. J. Hanisch, R. J. V. Brissenden, & J. Barnes, 173
- Vaughan, A. H., Preston, G. W., & Wilson, O. C. 1978, *PASP*, 90, 267, doi: [10.1086/130324](https://doi.org/10.1086/130324)
- Wakeford, H. R., & Sing, D. K. 2015, *A&A*, 573, A122, doi: [10.1051/0004-6361/201424207](https://doi.org/10.1051/0004-6361/201424207)
- Welbanks, L., Madhusudhan, N., Allard, N. F., et al. 2019, *ApJLett*, 887, L20, doi: [10.3847/2041-8213/ab5a89](https://doi.org/10.3847/2041-8213/ab5a89)
- Wilson, J., Gibson, N. P., & Nikolov, N. 2020, *MNRAS*, 999, 9999
- Wytttenbach, A., Lovis, C., Ehrenreich, D., et al. 2017, *A&A*, 602, A36, doi: [10.1051/0004-6361/201630063](https://doi.org/10.1051/0004-6361/201630063)

APPENDIX

A. SPECTROSCOPIC LIGHT CURVES

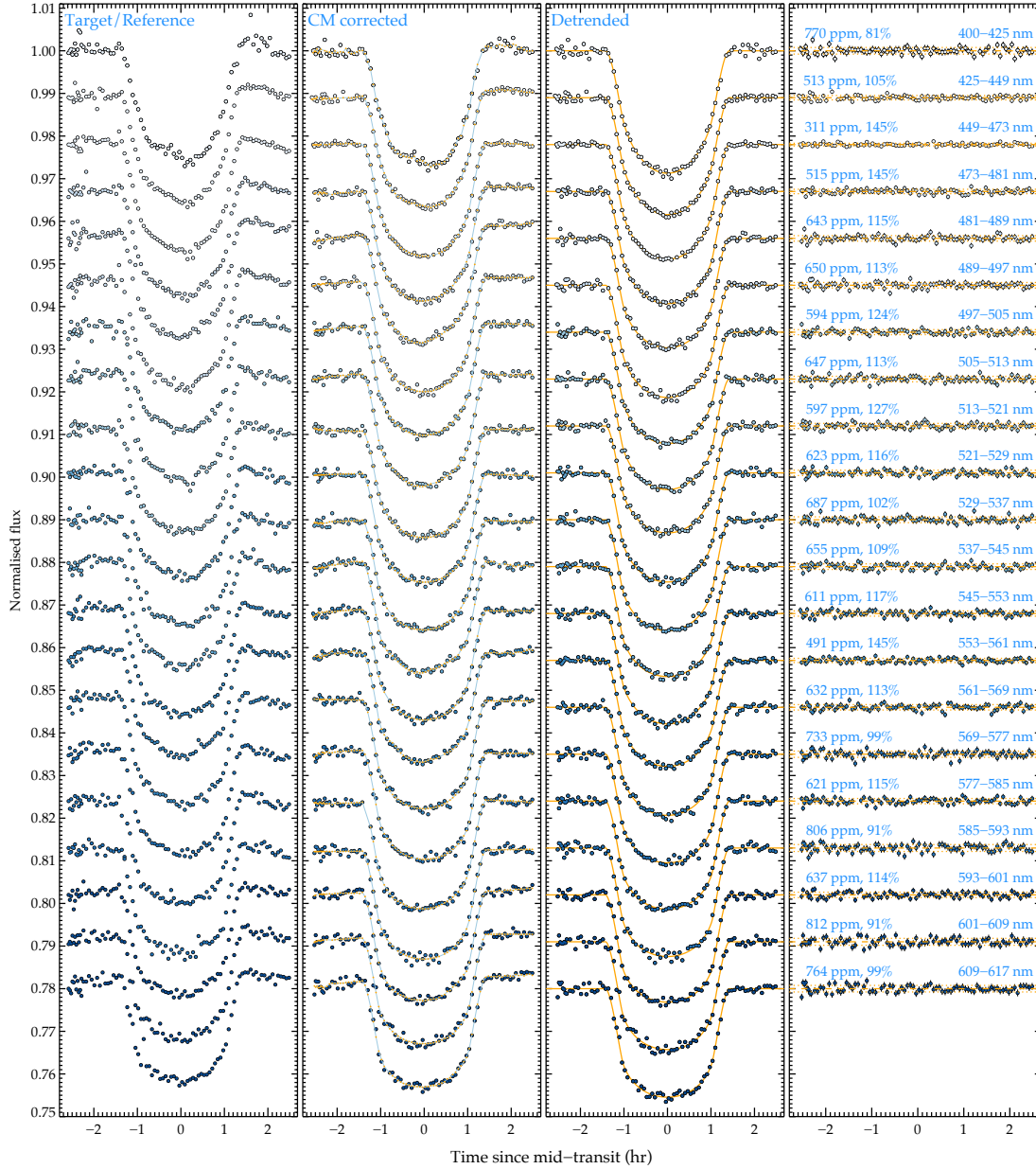


Figure 10. Spectrophotometric light curves from grism 600B offset by a constant amount for clarity. The first panel shows the raw target-to-reference flux. The second panel shows the common-mode (CM)-corrected light curves and the transit and systematics models, with the highest statistical weight. The third panel shows systematics corrected light curves and the transit model with the highest statistical weight. The fourth panel shows residuals with 1σ error bars. The dashed lines indicate the median residual level, with dotted lines indicating the dispersion and the percentage of the theoretical photon noise limit reached (blue)

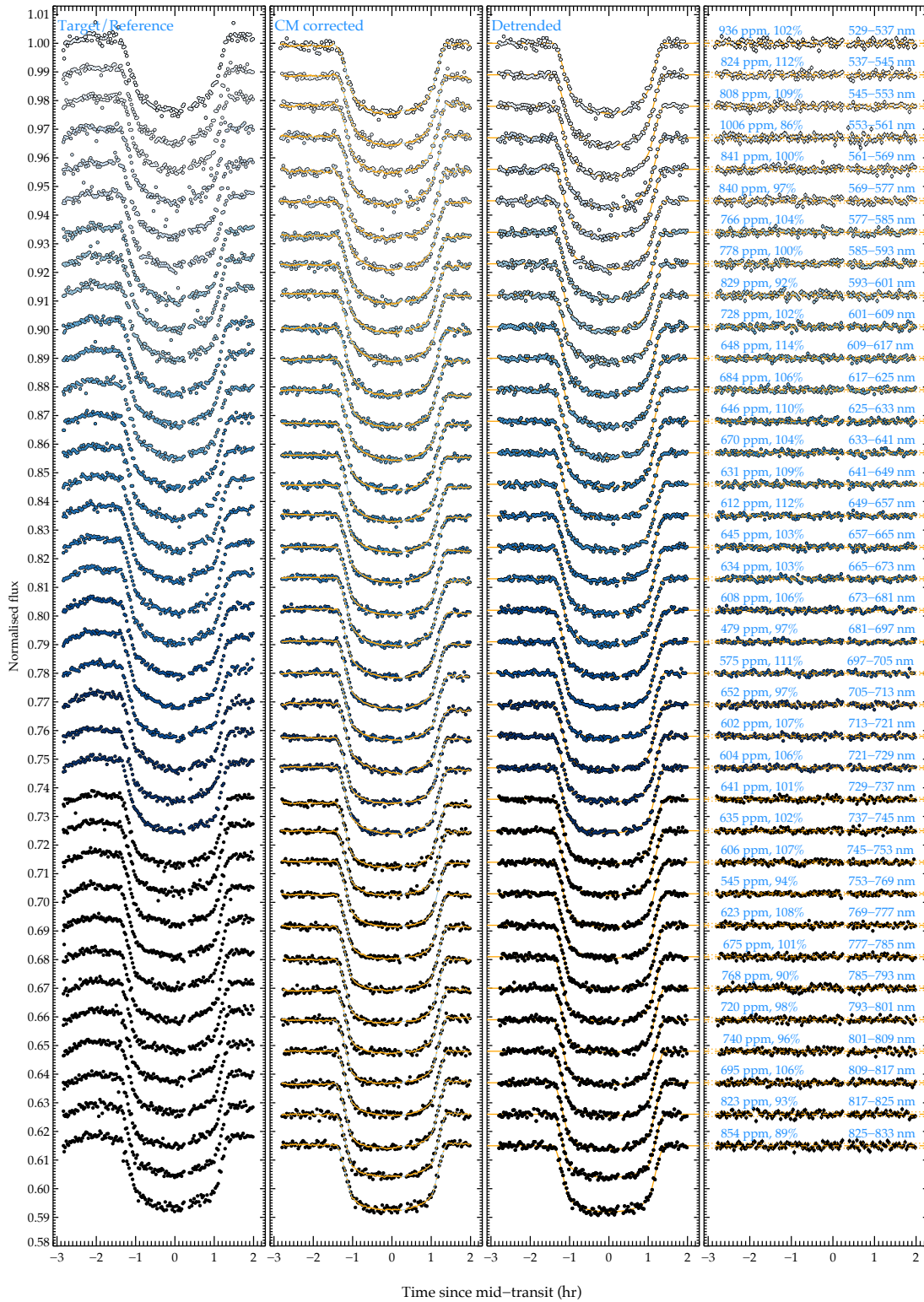


Figure 11. As for Figure 10 but for grism 600RI.

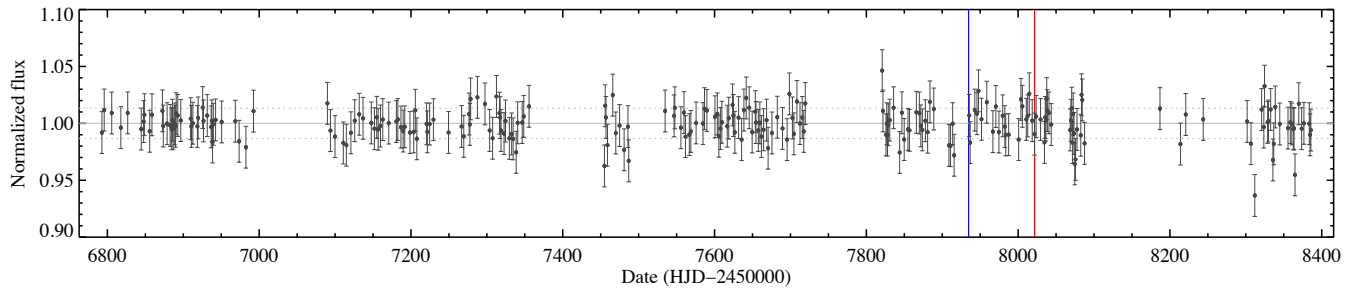


Figure 12. ASAS-SN light curve of WASP-110. The error bars indicate 1σ uncertainties. The vertical lines indicate the FORS2 GRIS600B (blue) and GRIS600RI (red) transit epochs, respectively. The horizontal lines indicate the mean and 1σ levels.

B. STELLAR VARIABILITY

C. RETRIEVAL RESULTS

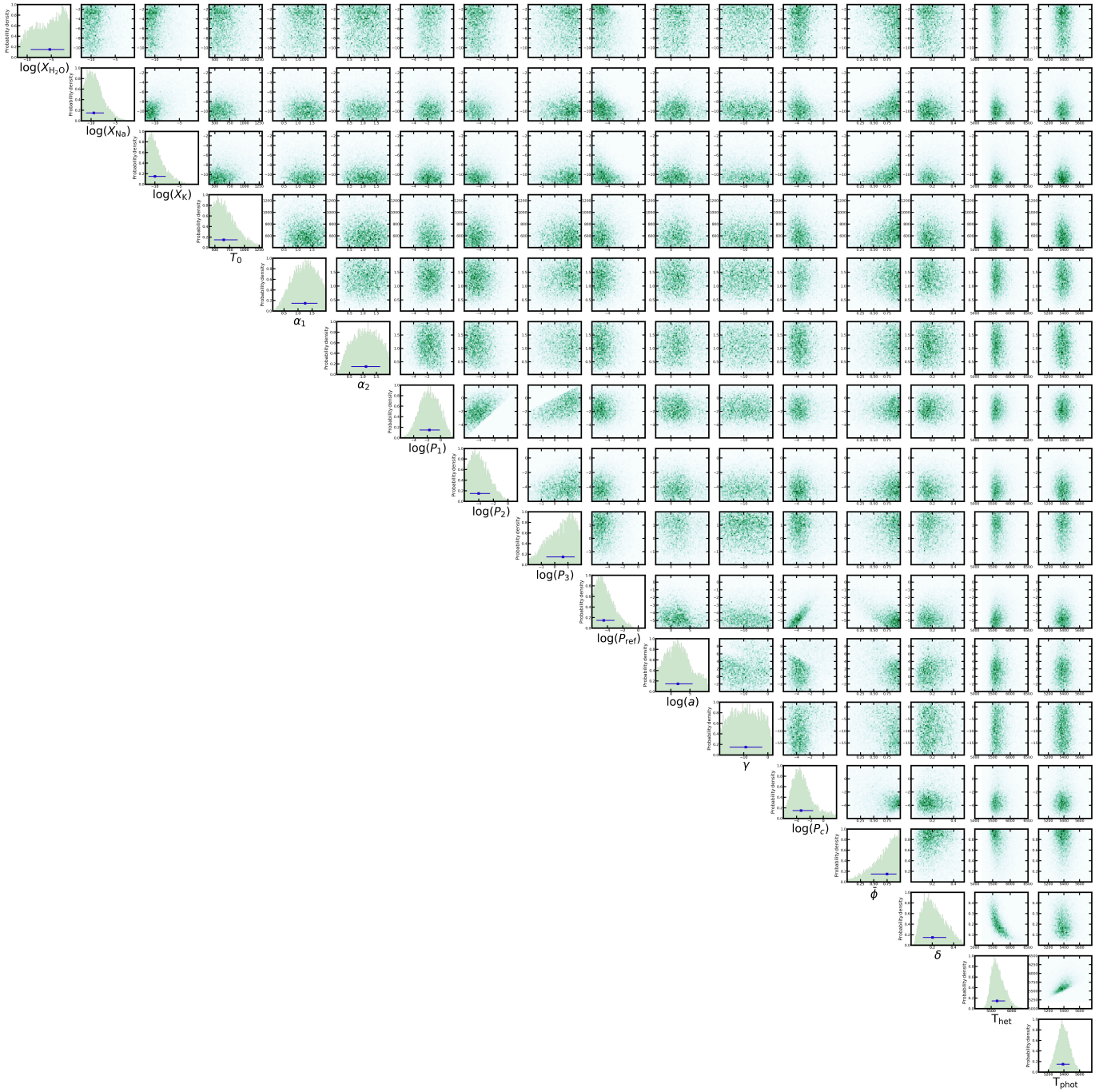


Figure 13. Posterior distribution obtained from our AURA retrieval, consisting of 3 chemical abundances, 6 pressure-temperature profile parameters, the reference pressure at the planetary radius, 4 clouds and hazes parameters and 3 stellar heterogeneity parameters.